🔓 **Open Access**

# Photo Scattering Signal Amplification in Gold-Viral Particle Ligation Towards Fast Infection Screening

Heng Zhang
Xiao Jin
Hanwen Zhao
Yongping Lin
Xiaofeng Li
Lianping Hou
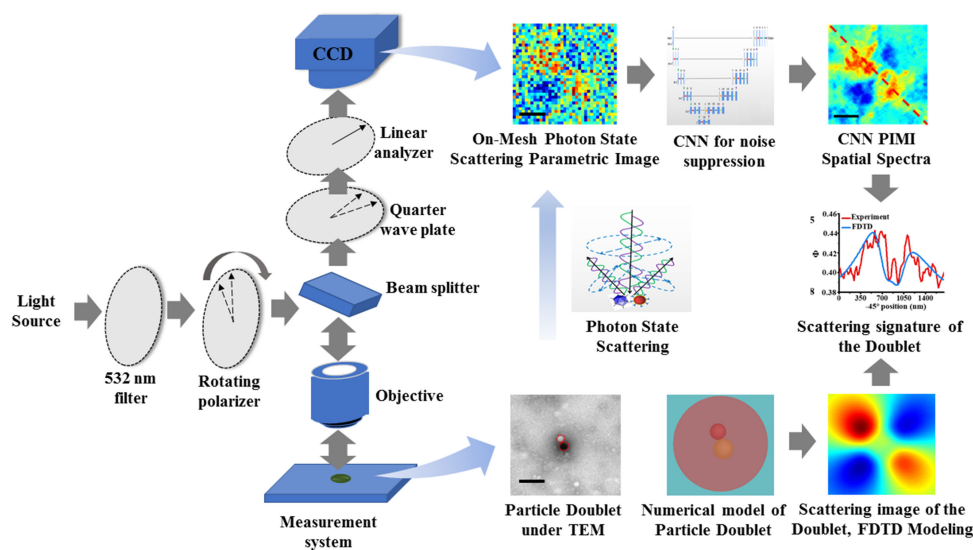John H. Marsh
Lei Dong
Daming Shi
Weiping Liu
Bin Xu
Bin Ni
Juan Liu
Jichuan Xiong
Xuefeng Liu

# Photo Scattering Signal Amplification in Gold-Viral Particle Ligation Towards Fast Infection Screening

**Heng Zhang,**[1] **Xiao Jin,**[1] **Hanwen Zhao,**[1] **Yongping Lin,**[2] **Xiaofeng Li,**[2]
**Lianping Hou** ,[3] **John H. Marsh** ,[3] **Lei Dong,**[4] **Daming Shi** ,[5]
**Weiping Liu,**[1] **Bin Xu,**[1] **Bin Ni** ,[1] **Juan Liu,**[1,6] **Jichuan Xiong** ,[1]
**and Xuefeng Liu** [1]

[1]School of Electronic and Optical Engineering, Nanjing University of Science and Technology, Nanjing 210094, China
[2]State Key Laboratory of Respiratory Disease, National Clinical Research Center for Respiratory Disease, Guangzhou Institute of Respiratory Disease, the First Affiliated Hospital of Guangzhou Medical University, Guangzhou Medical University, Guangzhou 510182, China
[3]James Watt School of Engineering, University of Glasgow, G12 8QQ Glasgow, U.K.
[4]School of Life Science, Beijing Institute of Technology, Beijing 100081, China
[5]College of Computer Science and Software Engineering, Shenzhen University, Shenzhen 518061, China
[6]Chinese Institute for Brain Research, Beijing 102206, China

**Abstract:** The polarization states of scattered photons can be used to map or image the anisotropic features of a nanostructure. However, the scattering strength depends heavily on the refractivity contrast in the near field under measurement, which limits the imaging sensitivity for viral particles which have little refractivity contrast with their nano-ambientes. In this paper, we show the photon scattering signal strength can be magnified by introducing a more abrupt change of refractivity at the virus particle using antibody-conjugated gold nanoparticles (AuNPs), allowing the presence of such viruses to be detected. Using two different deep learning methods to minimize scattering noise, the photon states scattering signal of a AuNPs ligated virus is enhanced significantly compared to that of a bare virus particle. This is confirmed by Finite Difference Time Domain (FDTD) numerical simulations. The sensitivity of the polarization state scattering spectra from a virus-gold particle doublet is 5.4 times higher than that of a conventional microscope image.

**Index Terms:** Polarization state, gold nanoparticles, virus, signal amplification.

## 1. Introduction

Viruses pose a huge threat to public health and the ability to detect them rapidly is of great importance for tracking and preventing pandemics such as COVID-19 [1]. Though much is now

known about the biological and pathogenic properties of many viruses, their ability to mutate quickly and the emergence of new infection agents can make it difficult to detect them rapidly [2].

Many virus detection methods have been developed, including: analysis of viral ribonucleic acid (RNA) based on the Reverse Transcription-Polymerase Chain Reaction (qRT-PCR), polymerase chain reaction (PCR) and enzyme-linked immunosorbent assay (ELISA) [3]; Loop-mediated isothermal amplification (LAMP) [4]; the CRISPR/Cas System [5]; immunochemistry [6]; and the detection of intact viral particles [7].

In techniques for the direct detection of RNA of viruses, many efforts have been made to amplify the signal including: detecting the miRNA with a programmable DNA-bridged nano-particle network (gold or quantum dots) [8]; chemiluminescence detection of spherical nucleic acid enzymes grown from AuNP@hairpin-DNA nanoprobes [9]; detecting surface plasmon-enhanced electrochemilu-minescence of one-to-one conjugation of RNA with gold nanoparticles [10]; or detecting the photoelectrochemical current signal from photoactive material connected to gold nanoparticles carrying antibodies [11]. In addition to antibody-conjugated gold nanoparticles (AuNPs), carbon and graphene quantum dots, which can be conjugated to RNA or DNA substrates have also been utilized for signal amplification in viral RNA detection [12]. Femtomolar sensitivity detection of RNA was achieved in voltammetry methods utilizing modified magnetic nanobeads (MBs) for signal enhancement [13].

Compared with the indirect methods described above, direct detection of the intact viral particles is more straightforward and shows potential for fast virus-screening applications, due to its versatility in detecting different kinds of virus and less stringent requirements for sample preparation. Solid state micro- and nanopores have been used to monitor viral particles in the air by detecting the cross-pore ionic current [14]. Electrolyte-gated field-effect transistors have been used as point-of-care (POC) devices for HIV detection, by transducing the bio-recognition event taking place at gate electrodes functionalized with the antibody [15].

Detection of intact viral particles with optical sensing methods is convenient and cost-effective. In the simple and widely used colloidal gold detection technology, virus-targeting molecules are intercalated into aggregated AuNPs, which have been functionalized to carry antibodies or nucleic acids. The absorption spectrum of aggregated AuNPs around virus-like particles (VLPs) has been utilized to detect the viruses [16]. Recently, portable platforms based on Raman spectroscopy have been developed to identify viral particles by analyzing their size [7]. Detection of Salmonella virus was achieved using a smartphone to analyze images of Fe-nanocluster amplified Prussian Blue staining of the sample [17]. Smartphone-based colorimetry was also implemented for avian influenza virus detection [18].

These optical methods mainly used AuNPs as functionalized labels to enhance the shift of the localized surface plasmon resonance (LSPR). The optical sensing of virus is based on the detection of the resonance spectrum from AuNP labeled virus and the sensitivity is accordingly dependent on the plasmonic emission intensity. Moreover, nonspecific binding of AuNPs to other components in the heterogeneous media or the formation of aggregates remains a challenge, along with the inconstancy of the fluorescence signal, which is dependent on the size of the biological nanoparticles. Images of plasmonic emission from virus-AuNPs complexes carry rich information that can be exploited for highly sensitive detection of virus. In our previously published papers, we have investigated the capability of polarization indirect microscopic imaging (PIMI) in resolving nano-features and molecular structures from the spatial polarization status distribution in the nano scattering field [19], [20]. It is found that the polarization states of the photons can be used to map or image the anisotropic features of the nanostructure, with a resolving power beyond the diffraction limit of conventional microscopy, by detecting the variation of coupling and scattering photon states from the sample [21], [22]. However, the scattering strength heavily depends on the change in refractivity in the near field under measurement. This limits imaging sensitivity for nano particles as it is not possible to identify the minor contrast between a virus particle and a biological environment with almost the same refractivity, especially in the presence of noise scattered from many other discontinuities. In this paper, we show the PIMI scattering strength can be magnified by introducing a more abrupt change of refractivity at the virus particle, so the signal
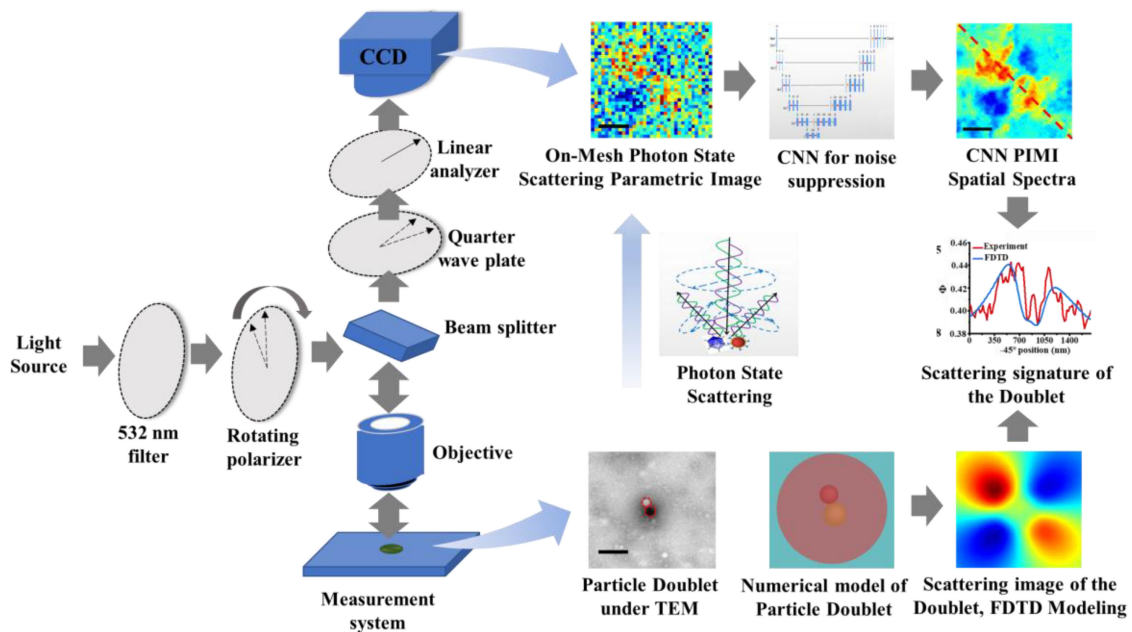
Fig. 1. Experimental setup and proposed mechanism of antibody-conjugated AuNPs for single virus detection, using photon state parametric indirect microscopic imaging (PIMI) optics and results, deep learning to suppress noise in the PIMI scattering images and comparison with simulated PIMI scattering via FDTD modeling.

is sufficiently large to determine the presence of the virus. To do this, we measured PIMI scattering from gold-virus doublets. This novel approach plays to the strength of the high sensitivity of PIMI images to anisotropy of the samples. However, the original mage, before processing, was always accompanied by heavy noise, which seriously affected the analysis. A denoising process therefore becomes essential. In recent years, deep learning techniques have developed rapidly for many applications including image denoising. Devalla *et al.* proposed a deep convolutional code-decode network for image denoising [23]; Bepler *et al.* use a deeper network structure and residual learning algorithm to improve the denoising performance [24]. Manifold *et al.* proved that neural networks can also learn to recognise self-similarity between images [25]. Inspired by work of Ledig *et al.* [26], we used a generative adversarial network to denoise the original images. By analyzing symmetric features in the spatial spectra of the PIMI images, the gold nanoparticles connected with a virus can be distinguished with high sensitivity from those not attached to a virus, providing a solution to the sensitivity issue for virus screening.

## 2. Measurement Mechanism of New Spatial Scattering Features of Virus-Gold Particles

The proposed system for using antibody-conjugated AuNPs as functional labels to identify single viruses is shown in Fig. 1. The AuNPs were synthesized by the Turkevich method [17]. Since adenovirus has multiple recognition sites for probes on its surface, the AuNP-hAb probes are arranged at specific sites on the virus surface due to their antigen recognition. After combining with virus, the PIMI scattering spectra of AuNPs changes dramatically. Deep learning methods were then used to suppress noise in the PIMI scattering images and the intensity profiles of the scattering dipoles were plotted as signature signals. The existence of virus could be determined by analyzing variational differences in the spatial scattering spectra, with the possibility of identifying a single virus.

PIMI is a far-field indirect imaging technique that can resolve anisotropic features in samples with high resolution and contrast. In PIMI imaging, the sample is illuminated by light with rotating polarization and the scattering spatial distribution varies due to different coupling between the illuminating light and the anisotropic features of the sample. The intensity variation detected by individual image pixels corresponding to each object point can be fitted to a sine curve. By fitting and filtering the intensity variations of the image pixels, a set of parametric images can be obtained in which the spatial resolution is greatly enhanced [20].

As shown in Fig. 1, the experimental system was based on a conventional reflection microscope (Olympus BX51). A 532 nm filter and a polarizer fixed on a motor were inserted after the white light source to provide a source of rotating polarized illumination. A quarter-wave plate and a linear analyzer with fast axes oriented at 45° and 90° respectively relative to the x-axis were placed in front of the imaging plane. A highly sensitive CCD (PiA2400-17gm, Basler) with 5 million pixels combined with a $100\times$ objective lens was used, making it possible to obtain images in which the pixel size corresponded to 34.5 nm.

The far-field optical image of the surface plasmon of AuNPs illuminated by the polarized light shows a distinct spatial distribution which reflects the structure of the AuNPs. This spatial distribution can be utilized to detect virus connected to the AuNPs.

## 3. Virus Labeled by AuNP-hexon Complex (AuNP-hAb) Probe

In the experiments of this paper, adenovirus was used as the virus sample for detection. Adenovirus is a type of icosahedral virus that can infect the respiratory tract, gastrointestinal tract, urethra, bladder, eyes and liver. Neutralizing Ab responses to adenovirus are directed at components of the virion surface, primarily against fiber, penton base, and hexon. Fiber and penton-based proteins, present at the vertices of the capsid, are involved in cell attachment and entry. Hexon, the major component of the icosahedral virus particle, comprises the facets of the virion and constitutes the bulk of the icosahedral capsid [27]. Attributing the binding affinity of the AuNP-hAb probe to adenovirus, it was expected that the probes would attach to the virus in positions corresponding to the recognition site.

The adenovirus was purchased from Hanbio Biological Technology Co. Ltd. Rabbit anti-Adenovirus hexon protein antibody (hAb) was purchased from Beijing Biosynthesis Biotechnology Co. Ltd (catalog number: bs-12354R). $HAuCl_4 \cdot 3H_2O$ was purchased from Sigma-Aldrich Co. Ltd. Other reagents were purchased from Sinopharm Group Chemical Reagent Co. Ltd. All commercially available reagents were used directly without any further purification. In all experiments, deionized Millipore water (18.25 $M\Omega$ cm$^{-1}$) was used.

In order to modify the surface of gold with antibodies, we prepared multilayer AuNP-polyelectrolyte nanoparticles using a layer-by-layer assembly approach by sequentially coating negatively charged polystyrene sulfonate (PSS) onto the AuNP-CTAB. The process is described in the literature [28]. Measurement of the particle size distribution showed that the synthesized AuNP-CTAB has a mean diameter of 84.7 $\pm$ 0.3 nm. It is worth noting that different polymers on the surface of the AuNPs did not cause any change in the macroscopic morphology (data not shown). The zeta potential of AuNP-CTAB ($+26.9 \pm 0.9$ mV) flipped from positive to negative, further confirming the successful surface passivation of AuNP-PSS ($-45.4 \pm 2.6$ mV). The higher surface charge resulted in repulsion and ensured a homogenous dispersion of AuNPs.

The antibodies were probably conjugated to the AuNP-PSS by a mechanism similar to that when antibodies bind to nanospheres, i.e., through an electrostatic physisorption interaction [29]. Next the prepared AuNP-hAb probes were used to capture the adenovirus.

Scanning electron microscopic (SEM) images were collected by a JSM-IT500HR. Transmission electron microscopic (TEM) images were taken at 200 kV on a JEM-2100. The hydrodynamic size and surface charge of the AuNPs in water were measured using a Zetasizer Nano ZS90 system. All data were averaged and expressed as the "mean $\pm$ SD". Here SD means standard deviation.
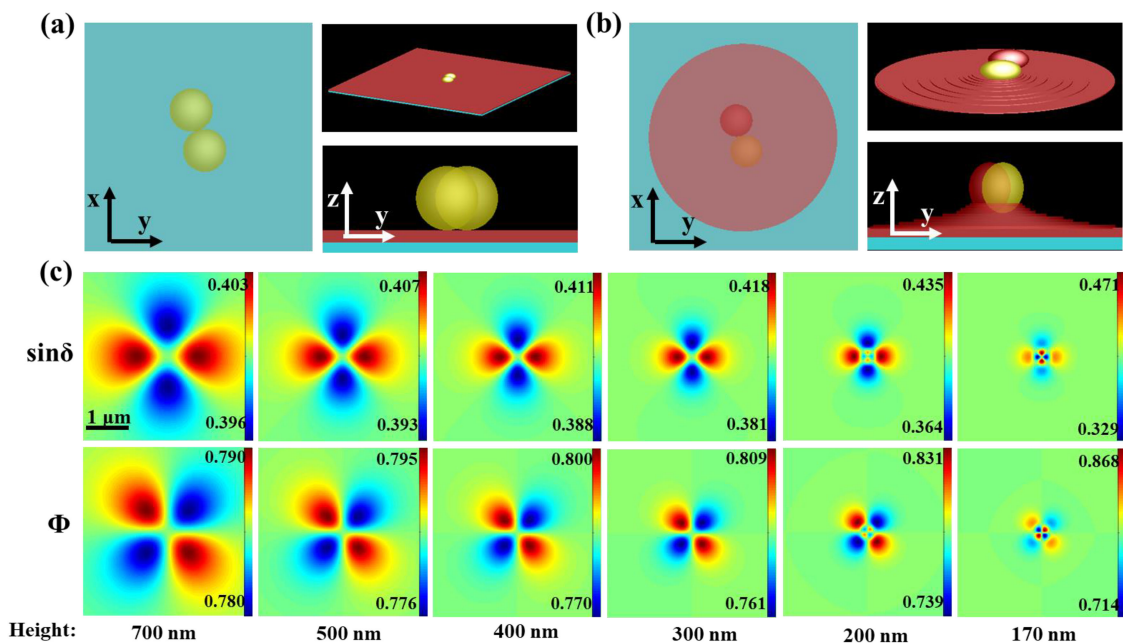
Fig. 2. (a) Structure of double AuNPs used in the simulations, (b) structure of AuNP-virus used for simulations, and (c) simulated PIMI images of a single AuNPs at different heights above the substrate surface.

## 4. Results and Discussion

### 4.1 Simulate Scattering Patterns of Different Structures

The capability of PIMI in resolving nano-features and molecular structures was investigated by using spatial polarization status distributions in the nano scattering field. Bare virus particles were almost invisible due to the similar refractivity of the virus particles and the surrounding biological environments. Therefore, metallic nanoparticles (AuNPs) were introduced to magnify the PIMI scattering strength, giving a sufficiently large signal for the presence of virus to be detected.

To investigate the theoretical photon state scattering patterns of single AuNPs, double AuNPs and AuNP-virus doublet, these three kinds of structure were at first numerically simulated. The simulation was based on FDTD solutions of Maxwell's equations. Here we simulated the electric field of AuNPs excited by polarized light. The structure comprised a 4 $\mu$m (length) $\times$ 4 $\mu$m (width) $\times$ 30 nm (height) carbon film substrate and single or double AuNPs with a diameter of 80 nm lying at the center of the substrate surface (Fig. 2(a)). It is worth noting that the simulation parameters for single AuNPs were the same as the parameters for double AuNPs. A structure consisting of an 80 nm ball with refractive index of 1.47 adjacent to a 100 nm AuNP was used to simulate AuNP-virus (Fig. 2(b)). We also included a 10 nm deposited layer of phosphotungstic acid to simulate the effect of negative staining in the TEM image procedure. A total-field scattered-field (TFSF) source with a wavelength of 532 nm was placed above the AuNP and the virus samples.

The polarization angle was increased in steps of 18° and the data for polarization angles (relative to the x-axis) from 0° to 162° for a particular height were collected. The initial data set therefore consisted of ten (162/18 + 1 = 10) images from which the PIMI images were then calculated (Fig. 2(c)). We recorded six sets of data for heights from 170 nm to 700 nm (relative to the substrate surface) to determine the field distribution of the light scattered from the single AuNPs.

In Fig. 2(c), the simulated PIMI images at different heights above a single gold particle are shown. From the intensity image sets, we can see the scattering field spreads out with increasing height. Some particle-size features at the center of the scattering field disappear rapidly when the
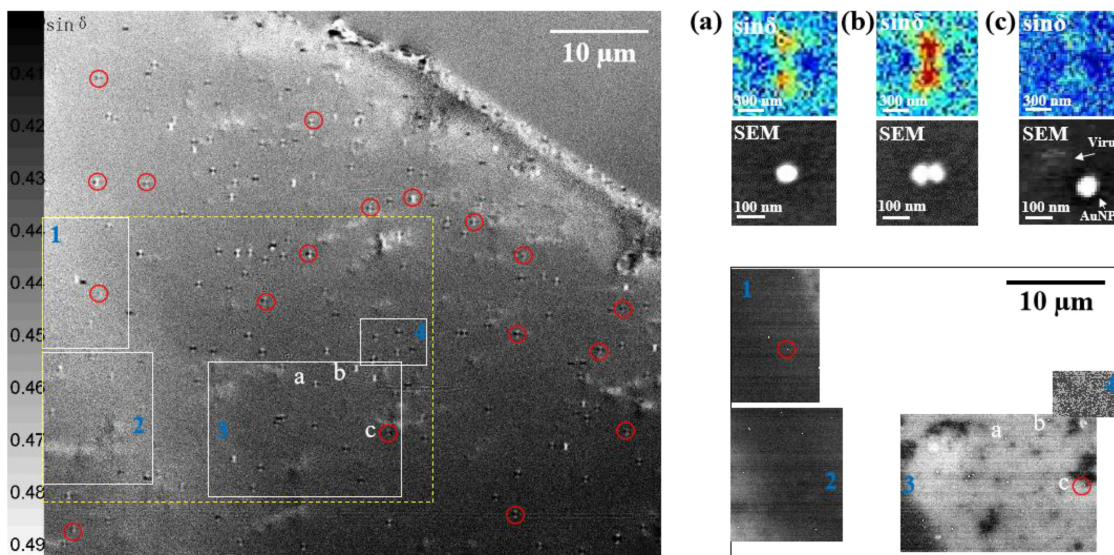
Fig. 3. Comparison of images for different structures. (a) single AuNPs, (b) double AuNPs, and (c) AuNP-virus. Left part is the PIMI sin$\delta$ image of the whole field (red circles represent possible AuNP-virus doublet), bottom right shows the corresponding SEM images of the rectangular regions marked in the left PIMI image.

height above the substrate surface is more than a half wavelength ($\sim$270 nm). The PIMI image reveals this characteristic more clearly for the two-dipole structure. In the sin$\delta$ image, there are two symmetric dipoles perpendicular or parallel to the initial polarization angle (0°). Similarly, there are two symmetric dipoles rotated 45° in the $\Phi$ image compared to the sin $\delta$ image.

The ideal image plane is the cross section through the center of the AuNPs, at which plane information carried by the near-field electromagnetic field is fully reflected in the PIMI images. However, considering the diffraction limit of the optical system and case of the focusing error in the experiment, simulated PIMI results for heights from 300 nm to 700 nm were used for comparison with the subsequent experimental results.

### 4.2 Detection of Adenovirus With AuNPs-hAb

The PIMI scattering of a gold-virus doublet was measured, followed by scanning electron microscopy (SEM) imaging of the same sample. The locations with scattering features similar to the simulated images were examined in detail with the SEM, to verify the existence of single AuNPs, double AuNPs and AuNP-virus. The SEM images shown in Fig. 3 confirm that the differences in photon scattering distributions seen in the PIMI images are due to the different particle structures at the corresponding locations, i.e., single AuNPs, double AuNPs, AuNP-virus. However, SEM imaging relies on the excitation of secondary electrons from the surface of the sample. Biological samples have weak electrical conductivity, which results in the excitation of only a few secondary electrons. As can be seen in the SEM image of the AuNP-virus particle (Fig. 3(a)), the signal intensity of a viral particle is much weaker than that of a AuNPs particle. Transmission electron microscopy (TEM) was therefore used instead of SEM, to verify the existence of and investigate the detailed structural configuration of the gold-virus doublets.

As shown in Fig. 4, visible scattering images with noise were obtained from the PIMI system over the whole field of view. A noisy but visible scattering image of the AuNPs ligated virus could be see using the bright-field PIMI system. Two parallel methods were used to increase the resolution and reduce the noise: a method based on self-similarity-encoded deep learning and a generative adversarial network (GAN) in which simulated results as the ground truth were applied separately.
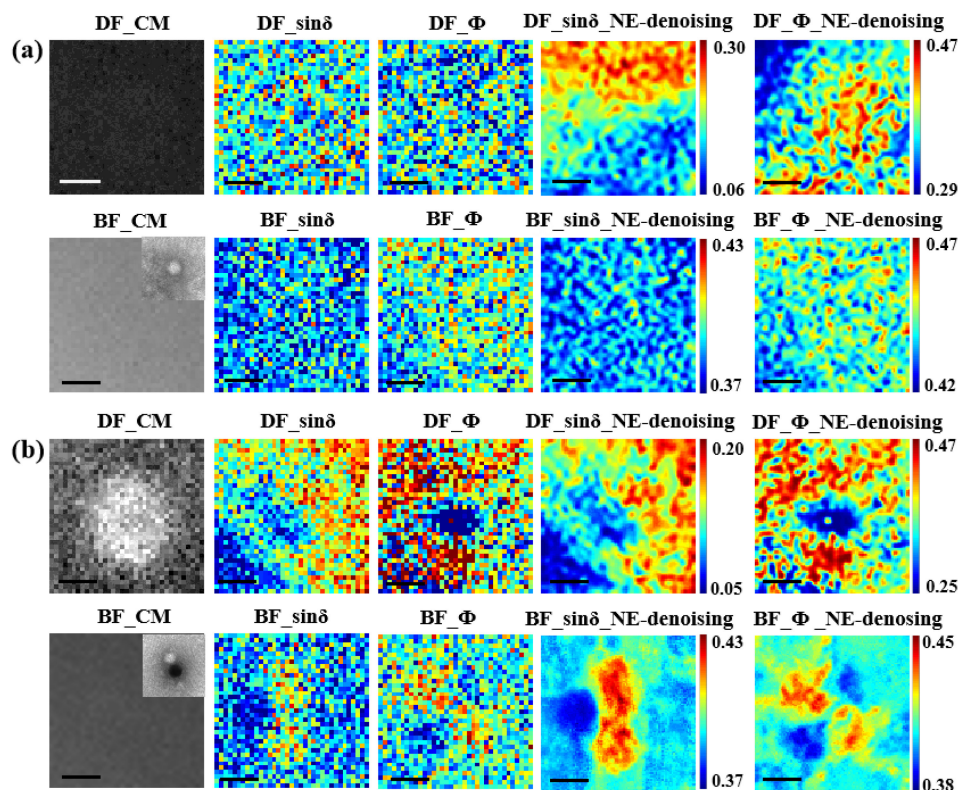
Fig. 4. Comparison of different structural images of (a) single virus and (b) AuNP-virus. DF: Means dark field, BF: Bright field, CM: Conventional wide-field optical microscope. The insets in the upper right corner in the CM images are the corresponding TEM images. The scale bars represent 300 nm.

In the self-similarity based neural-encoded (NE) deep learning method, we used 16 layers of random code Z as the input to a U-shaped generating network, and the parametric images with noise were mapped directly through the network. The gradient descent algorithm was used to obtain the optimal network parameters without the need for a ground truth. After a certain number of learning epochs, we used the network's priori and self-similarity of the parametric image to reduce the noise and improve the resolution of the experimental PIMI images.

In Fig. 4, no virus particles can be seen using conventional microscopy. They are also barely visible in PIMI images when the sample is located on a carbon film or silicon substrate. After combining with AuNPs, strong scattering of the nano field surrounding the virus-gold doublet was observed because of the abrupt change of refractivity. By comparing the four different structures: single virus, AuNP-virus, single AuNPs, and double AuNPs, it was found that such scattering areas were spatially distributed uniquely with both positive and negative dipoles. The symmetry of the AuNPs-virus doublet is rotated from that of a single gold particle and differs from the AuNPs doublet with one arm much stronger than the other one for both positive and negative dipoles.

As it is a method commonly used to detect nanoparticles, dark-field imaging was carried out in parallel with the bright field-imaging for each sample and the results are shown in Fig. 4 and Fig. 5. The conventional dark-field images of each sample do show a brighter spot than in the corresponding bright-field images, but the dark-field PIMI images do not show any regular pattern of dipoles corresponding to the structure of the sample, as is seen in the bright-field PIMI images. This may be due to the complex nano-ambientes of the particles, i.e., particles situated on a carbon film supported by a copper net, having a complex influence on the polarization states of the scattering photons. We have therefore not discussed dark-field imaging further.
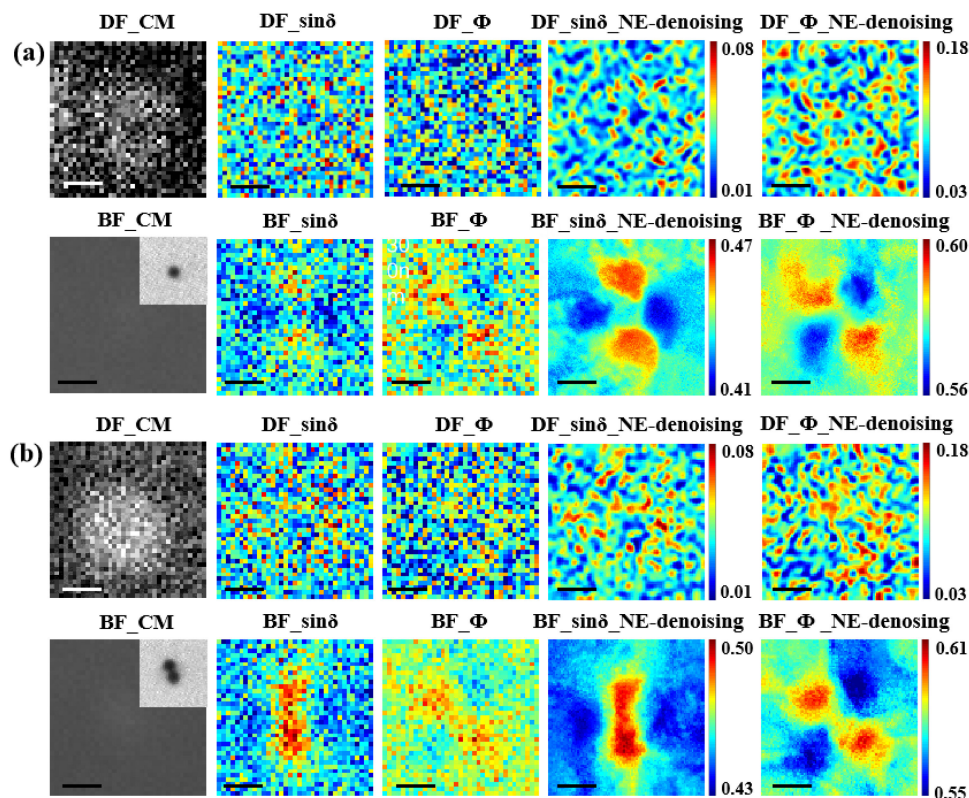
Fig. 5. Comparison of different structural images of (a) single AuNPs and (b) double AuNPs. DF: Means dark field, BF: Bright field, CM: Conventional wide-field optical microscope. The insets in the upper right corner in the CM images are the corresponding TEM images. The scale bars represent 300 nm.
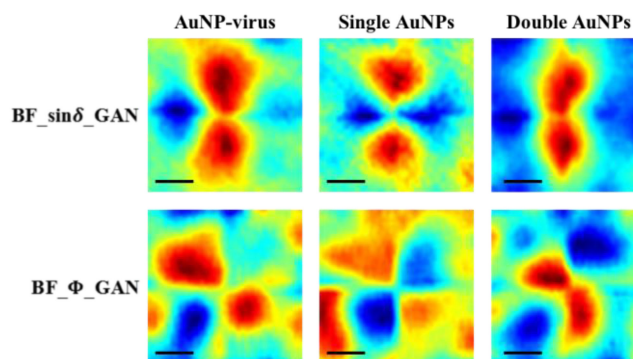


Fig. 6. Denoised images of AuNP-virus, single AuNPs and double AuNPs based on a generative adversarial network (GAN). The scale bar represents 300 nm.

To obtain a better understanding of the photon states scattering signals of metallic particles with similar size, but different refractivity from the viral particle, bright-field and dark-field systems PIMI images of single AuNP and double AuNPs are shown in Fig. 5. In the dark-field PIMI images, we still cannot identify a regular scattering pattern, although a diffraction spot can be seen, and the PIMI images of single AuNP and double AuNPs differs dramatically due to the change in structure and refractivity in the near field.

In Fig. 6, the bright-field PIMI images of AuNP-virus, single AuNPs and double AuNPs were further improved using a generative adversarial network (GAN). The network was trained using raw images of the sample under different illumination polarizations and FDTD simulations were
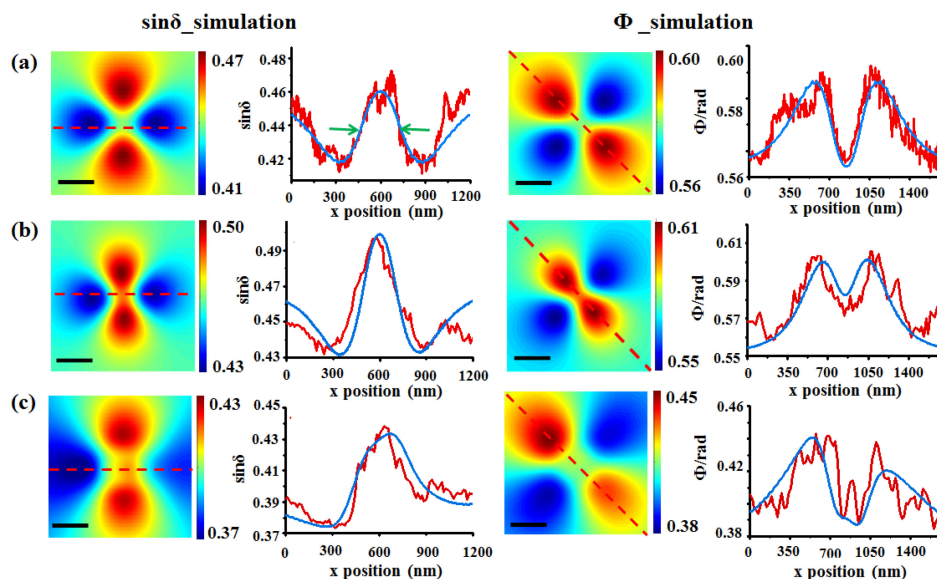
Fig. 7. Simulated PIMI images of (a) a single AuNPs, (b) double AuNP (b), and (c) AuNP-virus. The red line and blue line indicate experimental data and FDTD data respectively.

used as the ground truth. The deep neural network was trained following the GAN framework, in which two sub-networks are trained simultaneously; a generative model which converts the PIMI image to an FDTD-simulated image and a discriminative model which returns an adversarial loss to the PIMI-to-FDTD image. After processing with the GAN, the parametric images show clear spatial distributions of the scattering photons from the sample. The symmetry of scattering dipoles of the AuNP were considerably modified by the combination of virus to the AuNP. The improved contrast and signal to noise ratio of the PIMI images indicates that the FDTD simulated ground truth can train the network efficiently.

The conventional microscope image of the 80 nm particle was a blurred spot with size of about 600 nm, in which it was hard to distinguish the single gold particle from other small impurities or noise due to the diffraction limit and weak scattering light captured by the imaging system. The PIMI method is more powerful for detecting AuNPs in complex and dirty environments than conventional microscopy.

## 4.3  Quantification of Detection Sensitivity

As shown by the characteristic curves in Fig. 7, the experimental results are in good agreement with the FDTD simulations. The abscissa represents the position (from left to right) along the dotted line in each of the simulated PIMI images. The ordinate represents values of $\sin\delta$ and $\phi$ respectively. The FWHM (full width at half maximum) of the characteristic curves of a single AuNP is about 250 nm.

In Fig. 8, images of AuNP-virus for conventional microscopy (I00), PIMI $\sin\delta$ without GAN denoising, and $\sin\delta$ after GAN denoising are shown with the same colormap, together with the corresponding characteristic curves.

In Fig. 8, the I00 image shows a nonuniform intensity distribution in which barely visible features of a AuNP-virus can be seen, which may be due to the uneven scattering of the asymmetric structure of the AuNP-virus sample. In the PIMI $\sin\delta$ image, the symmetry of the scattering dipoles of the AuNPs are significantly modified by the combination of virus to the AuNPs. The nonuniform distribution caused by the light intensity disappears and a visible pattern related to the structure of the AuNP-virus doublet can be observed. To quantify the detection sensitivity of the method,
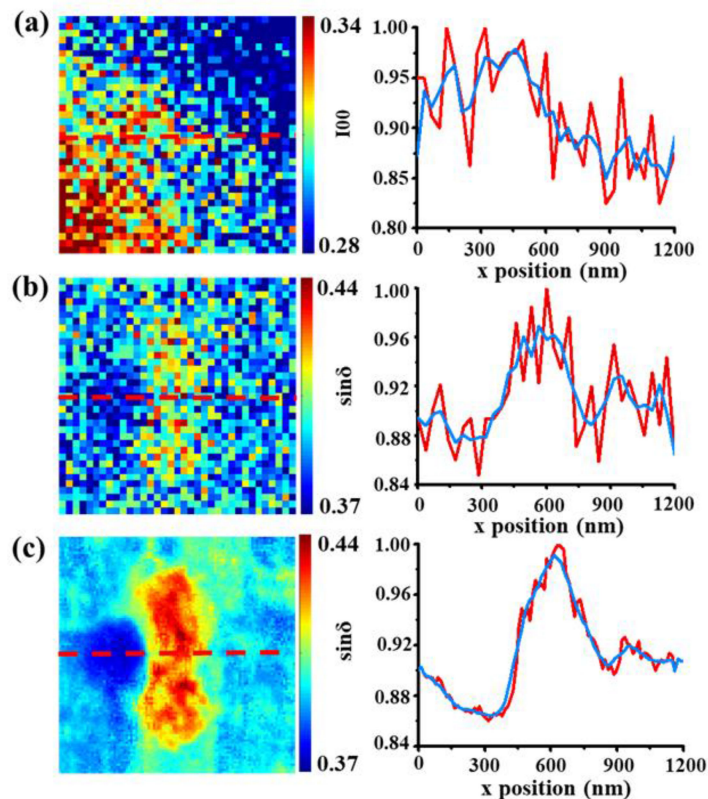
Fig. 8. Conventional (I00) image, PIMI image, PIMI image after GAN denoising and their characteristic curves: (a) AuNP-virus for I00, (b) sin $\delta$ image without GAN denoising, (c) sin $\delta$ image after GAN denoising. The red line and blue line indicate experimental data and mean filter data respectively.

the peak signal-to-noise ratio (PSNR) of the characteristic curves were used. A mean filter on a 100 nm-scale was used to smooth the curves and then the PSNRs of the curves were calculated. The PSNRs for Fig. 8(a), (b) and (c) are 29.11 dB, 31.57 dB, and 43.80 dB respectively. The sensitivity of the sin$\delta$ image after GAN denoising is about 5.4 times higher than that of the conventional microscopy (I00) image.

## 5. Conclusion

In this work, we report the spatial scattering spectra of adenovirus labeled with AuNP-hAb by the PIMI method. The detailed characterization of adenovirus using PIMI showed higher contrast than that possible using a traditional optical microscope. Spatial scattering spectra of photon state parameters have been found to be very sensitive to the presence of virus combined with gold nanoparticles. The virus with gold nanoparticles can be observed with great sensitivity in the spatial spectra of PIMI images, with experimental and numerical simulations showing good agreement. A more comprehensive way to quantify the asymmetric PIMI scattering distribution would be through direct analysis of the images themselves, rather than extracting characteristic curves at certain angles from the images. This could further improve the accuracy and sensitivity of our detection technique. In order to do this direct analysis, a deep learning neural network will use a large number of samples to identify the "fingerprints" associated with antibody-conjugated gold nanoparticles in the PIMI scattering images. These fingerprints could provide a possible way for rapid identification of virus in the future. In further research, we plan to systematically evaluate the reliability, efficiency, sensitivity and other performance parameters of the method by designing and fabricating a gold nanoarray with different structures. This approach is expected to provide more sensitive scattering

images and a route to high-throughput parallel detection. These techniques have the potential to detect low concentrations of virus or even a single virus.

# References

[1] M. Mofijur *et al.*, "Impact of COVID-19 on the social, economic, environmental, and energy domains: Lessons learnt from a global pandemic," *Sustain. Prod. Consump.*, vol. 26, pp. 343–359, 2021.

[2] L. Huang *et al.*, "Progress in the research and development of anti-COVID-19 drugs," *Front. Public Health*, vol. 8, p. 365, 2020.

[3] B. Chaharaein, A. R. Omar, I. Aini, K. Yusoff, and S. S. Hassan, "Detection of H5, H7, and H9 subtypes of avian influenza viruses by multiplex reverse transcription-polymerase chain reaction," *Microbiol. Res.*, vol. 164, no. 2, pp. 174–179, 2009.

[4] J. Cui, F. Li, and Z. L. Shi, "Origin and evolution of pathogenic coronaviruses," *Nat. Rev. Microbiol.*, vol. 17, no. 3, pp. 181–192, 2019.

[5] Q. He *et al.*, "High-throughput and all-solution phase African swine fever virus (ASFV) detection using CRISPR-Cas12a and fluorescence based point-of-care system," *Biosens. Bioelectron.*, vol. 154, 2020, Art. no. 112068.

[6] S. Wee *et al.*, "Multiplex targeted mass spectrometry assay for one-shot flavivirus diagnosis," *Proc. Nat. Acad. Sci. United States Amer.*, vol. 116, no. 14, pp. 6754–6759, 2019.

[7] Y. T. Yeh *et al.*, "A rapid and label-free platform for virus capture and identification from clinical samples," *Proc. Nat. Acad. Sci. United States Amer.*, vol. 117, pp. 895–901, 2020.

[8] R. Yue, Z. Li, G. Wang, J. Li, and N. Ma, "Logic sensing of microRNA in living cells using DNA-programmed nanoparticle network with high signal gain," *ACS Sens.,* vol. 4, no. 1, pp. 250–256, 2019.

[9] L. Shi, Y. Sun, L. Mi, and T. Li, "Target-catalyzed self-growing spherical nucleic acid enzyme (SNAzyme) as a double amplifier for ultrasensitive chemiluminescence microRNA detection," *ACS Sens.,* vol. 4, no. 12, pp. 3219–3226, 2019.

[10] T. Lee *et al.*, "Single functionalized pRNA/Gold nanoparticle for ultrasensitive microRNA detection using electrochemical surface-enhanced Raman spectroscopy," *Adv. Sci.*, vol. 7, 2020, Art. no. 1902477.

[11] M. Wang *et al.*, "Photoelectrochemical biosensor for microRNA detection based on a mos2/g-C3N4/black tio2 heterojunction with Histostar@aunps for signal amplification," *Biosens. Bioelectron.*, vol. 128, pp. 137–143, 2019.

[12] M. Li, T. Chen, J. J. Gooding, and J. Liu, "Review of carbon and graphene quantum dots for sensing," *ACS Sens.,* vol. 4, no. 7, pp. 1732–1748, 2019.

[13] W. J. Guo, Z. Wu, X. Y. Yang, D. W. Pang, and Z. L. Zhang, "Ultrasensitive electrochemical detection of microrna-21 with wide linear dynamic range based on dual signal amplification," *Biosens. Bioelectron.*, vol. 131, pp. 267–273, 2019.

[14] M. Tsutsui *et al.*, "Identifying single particles in air using a 3D-integrated solid-state pore," *ACS Sens.,* vol. 4, no. 3, pp. 748–755, 2019.

[15] S. K. Sailapu *et al.*, "Standalone operation of an EGOFET for ultra-sensitive detection of HIV," *Biosens. Bioelectron.*, vol. 156, 2020, Art. no. 112103.

[16] K. Niikura *et al.*, "Gold nanoparticle arrangement on viral particles through carbohydrate recognition: A non-cross-linking approach to optical virus detection," *Bioconjugate Chem.,* vol. 20, no. 10, pp. 1848–1852, 2009.

[17] H. Zhang *et al.*, "A capillary biosensor for rapid detection of salmonella using Fe-nanocluster amplification and smart phone imaging," *Biosens. Bioelectron.*, vol. 127, pp. 142–149, 2019.

[18] Y. Xia *et al.*, "Smartphone-based point-of-care microfluidic platform fabricated with a ZnO nanorod template for colorimetric virus detection," *ACS Sens.,* vol. 4, no. 12, pp. 3298–3307, 2019.

[19] K. Ullah, X. Liu, M. Habib, and Z. Shen, "Subwavelength far field imaging of nanoparticles with parametric indirect microscopic imaging," *ACS Photon.*, vol. 5, no. 4, pp. 1388–1397, 2018.

[20] K. Ullah, B. Garcia-Camara, M. Habib, N. P. Yadav, and X. Liu, "An indirect method of imaging the stokes parameters of a submicron particle with sub-diffraction scattering," *J. Quant. Spectroscapy Radiat. Transfer*, vol. 213, pp. 35–40, 2018.

[21] K. Ullah, X. Liu, A. Krasnok, M. Habib, L. Song, and B. Garcia-Camara, "Resolving the multipolar scattering modes of a submicron particle using parametric indirect microscopic imaging," *Photon. Nanostruct. Fundam. Appl.*, vol. 30, pp. 7–13, 2018.

[22] W. Liu, J. Xiong, H. Zhang, X. Liu, G. Liu, and H. Zhao, "Characterization of Komagataeibacter xylinus by a polarization modulation imaging method," *J. Phys. D Appl. Phys.*, vol. 53, no. 12, 2020, Art. no. 125403.

[23] S. K. Devalla *et al.*, "A deep learning approach to denoise optical coherence tomography images of the optic nerve head," *Sci. Rep.*, vol. 9, no. 14454, 2019.

[24] T. Bepler, K. Kelley, A. J. Noble, and B. Berger, "Topaz-Denoise: General deep denoising models for cryoEM and cryoET," *Nat. Commun.*, vol. 11, no. 5208, 2020.

[25] B. Manifold, E. Thomas, A. T. Francis, A. H. Hill, and D. Fu, "Denoising of stimulated Raman scattering microscopy images via deep learning," *Biomed. Opt. Exp.*, vol. 10, no. 8, pp. 3860–3874, 2019.

[26] C. Ledig *et al.*, "Photo-realistic single image super-resolution using a generative adversarial network," in *Proc. IEEE Conf. Comput. Vis. Pattern Recognit.*, pp. 105–113, 2017.

[27] V. S. Reddy and M. A. Barry, "Structural organization and protein-protein interactions in human adenovirus capsid," *Sub-Cell Biochem.,* vol. 96, pp. 503–518, 2021.

[28] N. A. Azman, L. Bekale, T. X. Nguyen, and J. C. Y. Kah, "Polyelectrolyte stiffness on gold nanorods mediates cell membrane damage," *Nanoscale*, vol. 12, no. 26, pp. 14021–14036, 2020.

[29] X. H. Huang, I. H. El-Sayed, W. Qian, and M. A. El-Sayed, "Cancer cell imaging and photothermal therapy in the near-infrared region by using gold nanorods," *J. Amer. Chem. Soc.*, vol. 128, no. 6, pp. 2115–2120, 2006.